J. Fluid Mech. (2024), *vol*. 995, A5, doi:10.1017/jfm.2024.670

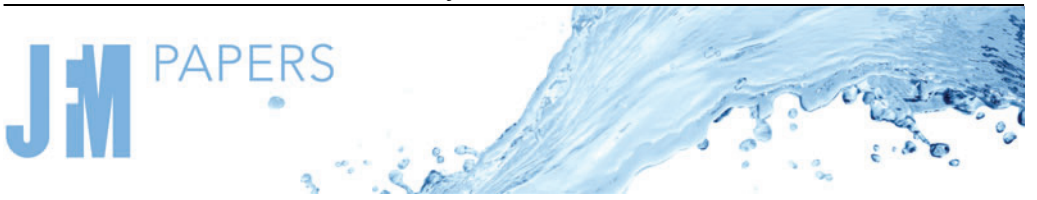

Instability dynamics of viscous fingering interaction on dual displacement fronts

Anindityo Patmonoaji[1,2,3,†], **Yuichiro Nagatsu**[2,†] **and Manoranjan Mishra**[4]

[1]Department of Earth Science and Engineering, Imperial College London, London SW7 2AZ, UK

[2]Department of Chemical Engineering, Tokyo University of Agriculture and Technology, Naka-cho 2-24-16, Koganei, Tokyo 184-8588, Japan

[3]Department of Mechanical Engineering, Tokyo Institute of Technology, 2-12-1 Ookayama, Meguro-ku, Tokyo 152-8551, Japan

[4]Department of Mathematics, Indian Institute of Technology Ropar, Rupnagar 140001, India

(Received 18 November 2023; revised 3 May 2024; accepted 29 May 2024)

We explored the instability dynamics of the viscous fingering interaction in dual displacement fronts by varying the viscosity configuration. Four regimes of rear-dominated fingering, front-dominated fingering, dual fingering and stable were identified. By using the breakthrough time, which refers to the breakup of the dual displacement fronts, the instability dynamics were modelled, and a regime map was developed. These serve as a tool for effectively harnessing the dual displacement fronts for various applications, such as hydrogeology, petroleum, chemical processes and microfluidics.

Key words: fingering instability, Hele-Shaw flows, porous media

1. Introduction

Viscous fingering (VF) or Saffman–Taylor instability (Saffman & Taylor 1958) occurs when a less viscous fluid displaces a more viscous fluid in porous media, Hele-Shaw cells or microfluidic cells. Since it was first reported by Hill (1952), extensive research investigations have been performed due to its widespread applications (Homsy 1987; De Wit 2020). Most of the reported works, however, are mainly on a single displacement front. Interests given to dual displacement fronts, in which two fluid interfaces are formed, are still limited despite their importance for various applications. Given the characteristics of dual displacement fronts, it can be harnessed in two opposite ways. The first is to generate efficient fluid displacement processes in reservoir treatment (Paraskeva *et al.* 2000; Talaghat, Esmaeilzadeh & Mowla 2009), enhanced oil recovery (Le Van & Chon 2017; Vishnudas & Chaudhuri 2017; Afzali, Rezaei & Zendehboudi 2018; Chaudhuri &

† Email addresses for correspondence: a.patmonoaji@imperial.ac.uk, nagatsu@cc.tuat.ac.jp

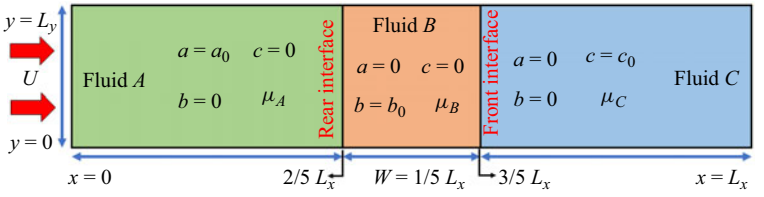

Figure 1. Sketch of the fluid configuration system.

Vishnudas 2018; Bakharev *et al.* 2022), *in situ* groundwater remediation (Wood, Simmons & Hutson 2004) and column chromatography (Mayfield *et al.* 2005; Shalliker *et al.* 2007; Shalliker & Guiochon 2010) for hydrogeology, petroleum and chemical processes. The second is to induce fluid mixing in a confined fluid system with a small Reynolds number for microdroplet generation (Cardoso & Woods 1995; Hashimoto *et al.* 2008) and microflow mixing (Glasgow & Aubry 2003; Coleman & Sinton 2005; MacInnes, Chen & Allen 2005) for various biological and chemical syntheses. To generate efficient fluid displacement, stable displacement should be maintained by avoiding VF (Yuan & Azaiez 2014; Sharma *et al.* 2021). In contrast, VF is desirable for enhancing the mixing process by breaking the stability (Jha, Cueto-Felgueroso & Juanes 2013; Chen *et al.* 2015). To the best of our knowledge, the exploration of these strategies is still an open question.

The first work on the dual displacement fronts was performed by De Wit, Bertho & Martin (2005), and afterwards, a series of similar studies were reported (Mishra, Martin & De Wit 2008, 2009, 2010; Hota, Pramanik & Mishra 2015). Some experimental studies have also been performed by utilizing micropillar array columns (De Malsche *et al.* 2009; Haudin *et al.* 2016). However, the analyses were mainly focused on the VF structure, the linear stability analysis and the mixing process, whereas analysis of the interaction dynamics of VF has never been discussed. In this paper, we explored the interaction dynamics of VF in dual displacement fronts through numerical simulation by varying the viscosity configuration. By using each interface onset time, finger velocity and the finite slice breakthrough time, we modelled and mapped the interaction dynamics of VF in dual displacement fronts with various viscosity configurations of the finite slice and bulk fluid.

2. Mathematical formulation and numerical solution

We consider miscible fluids A, B and C placed from left to right, forming two-fluid interfaces of AB and BC, referred to as the rear interface and the front interface, respectively. The fluid flow is considered in a two-dimensional porous medium with uniform porosity and constant permeability κ. Fluid A then flows to the right, pushing the dual displacement front configuration, as shown in figure 1.

With the assumptions that the system is incompressible, neutrally buoyant and first contact miscible, the governing equations are

$$\nabla \cdot \underline{u} = 0, \quad \nabla p = -\frac{\mu}{\kappa}\underline{u}, \tag{2.1a,b}$$

$$\frac{\partial a}{\partial t} + \underline{u} \cdot \nabla a = D_A \nabla^2 a, \tag{2.2}$$

$$\frac{\partial b}{\partial t} + \underline{u} \cdot \nabla b = D_B \nabla^2 b, \tag{2.3}$$

$$\frac{\partial c}{\partial t} + \underline{u} \cdot \nabla c = D_C \nabla^2 c. \tag{2.4}$$

In the above expressions, the fluid flow velocity $\underline{u} = (u, v)$, p is the pressure, μ is the fluid viscosity, t is time, a, b and c are the concentration of the fluids A, B and C, respectively. It is assumed that the diffusion coefficients of fluids A, B and C are the same, i.e. $D_A = D_B = D_C = D$. The initial concentration value of a is a_0, and subscripts A, B and C represent the parameters of fluids A, B and C, respectively. The viscosity concentration relation is considered as Arrhenius type (Hejazi *et al.* 2010; Hejazi & Azaiez 2012),

$$\mu = \mu_A \exp\left(\left(R_B \frac{b}{a_0} + R_C \frac{c}{a_0}\right)\right), \tag{2.5}$$

where, $R_B = \ln(\mu_B/\mu_A)$, and $R_C = \ln(\mu_C/\mu_A)$ are the log mobility ratios between the viscosity of B, C with A, respectively. The governing equations above were then non-dimensionalized by using injection velocity (U), hydrodynamical time ($\tau_h = D/U^2$) and length ($L_h = D/U$). Viscosity and pressure are normalized by μ_A and $\mu_A D/\kappa$, respectively. The concentration of species A, B and C are also scaled by a_0 (initial concentration of A). A reference frame moving with the injection velocity was used to focus on the dual displacement front dynamics. Afterwards, introducing a stream function $\psi(x, y)$ such that $u = \partial\psi/\partial y$ and $v = -\partial\psi/\partial x$, the model equations can be written in the stream function–vorticity formulation (Tan & Homsy 1988; De Wit *et al.* 2005), as

$$\nabla^2\psi = -R_B(\psi_x b_x + \psi_y b_y + b_y) - R_C(\psi_x c_x + \psi_y c_y + c_y), \tag{2.6}$$

$$a_t + a_x\psi_y - a_y\psi_x = \nabla^2 a, \tag{2.7}$$

$$b_t + b_x\psi_y - b_y\psi_x = \nabla^2 b, \tag{2.8}$$

$$c_t + c_x\psi_y - c_y\psi_x = \nabla^2 c, \tag{2.9}$$

$$\mu = e^{R_B b + R_C c}. \tag{2.10}$$

For the numerical simulation, dimensions of $L_y = 1024$, $L_x = 5120$ and $W = 1024$ (figure 1) were used. This slice width was selected because it gives enough space for the fingering development without the disturbance from the periodic boundary layer. In addition, it gives a reasonable computational time to observe the breakthrough time. We consider periodic boundary conditions in both the axial and transverse directions to avoid disturbances to the fluid flow. They do not affect the dual displacement front dynamics at the centre. An initial random disturbance was introduced to induce the instability. As reported by De Wit *et al.* (2005), this random disturbance magnitude mainly affects the VF onset time. Smaller random disturbance magnitude leads to longer onset time, resulting in unnecessarily longer computational time. Therefore, to ensure similar initial conditions and reasonable computational time, a constant value of random disturbance of $O(10^{-2})$ was selected throughout this work. Further, (2.6)–(2.10) are numerically solved using a Fourier pseudospectral method introduced by Tan & Homsy (1988), which has been shown to successfully model various numerical studies of VF (De Wit & Homsy 1999; Nagatsu & De Wit 2011).

For the quantitative evaluation, parameters based on the transverse average fluid concentration profile

$$i_{avg,y}(x, t) = \frac{1}{L_y}\int_0^{L_y} i(x, y, t)\,\mathrm{d}y, \tag{2.11}$$

with i corresponding to the concentrations (a, b and c) of fluid A, B or C were used (see figure 2). First, the mixing length (ML) in red of the fluids A and C defined as the length

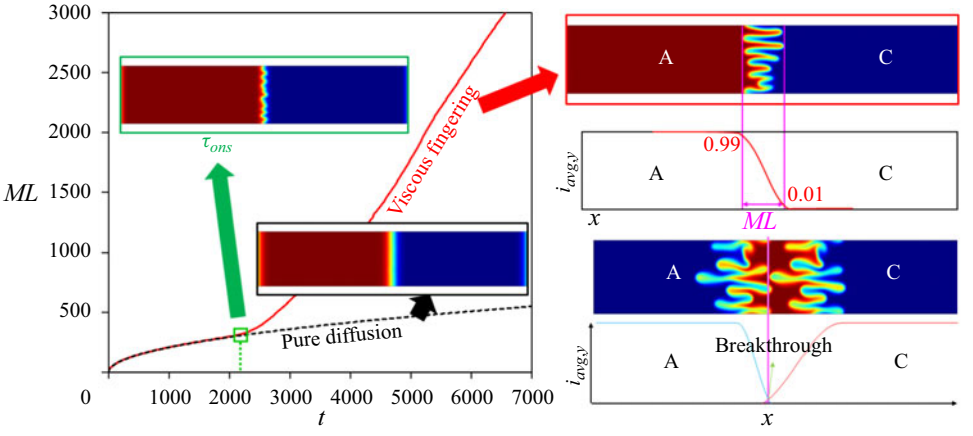

Figure 2. Sketch of the onset and breakthrough concepts.

between the transverse average fluid concentration of ϵ and $(\epsilon - 1)$ with $\epsilon = 0.01$ was obtained. Next, the deformation of the rear interface ($\tau_{ons,R}$) and the front interface ($\tau_{ons,F}$) were measured by comparing the mixing length with the pure diffusion case. The onset time is determined as the time when the mixing length starts deviating from the pure diffusive interface value by 10. Lastly, we introduced the breakthrough time τ_{bk} that was determined when any transverse average fluid concentration contained concentrations of both fluid A and C larger than ϵ, indicating the breakthrough of fluid B slice (see figure 2). Once the fluid B slice has broken through, the dual displacement fronts become inefficient for displacement (Paraskeva *et al.* 2000; Wood *et al.* 2004; Mayfield *et al.* 2005; Shalliker *et al.* 2007; Talaghat *et al.* 2009; Le Van & Chon 2017; Vishnudas & Chaudhuri 2017; Afzali *et al.* 2018; Chaudhuri & Vishnudas 2018; Bakharev *et al.* 2022) but effective for fluid mixing (Coleman & Sinton 2005; MacInnes *et al.* 2005; Jha *et al.* 2013; Chen *et al.* 2015). Therefore, this parameter is used as the main indicator in characterising the dual displacement fronts instability dynamics.

3. Results and discussion

Simulations with $R_C = 2$, $R_C = 0$ and $R_C = -1$, representing the condition of $R_C > 0$, $R_C = 0$ and $R_C < 0$ were performed with varied R_B. This helps to compare the results when the viscosity of displacing fluid A is more, the same or less than the viscosity of displaced fluid C. Simulations are performed for five different random numbers generated for the seeding of the instability in each set of parameters. In order to find the onset of deformation, we computed the evolution of mixing length for several R_B and $R_C = 2$, 0 and -1, with the same initial condition and plotted in figure 3. The examples of mixing length development for all R_B and R_C at one randomness case are shown. The onset of instabilities of both frontal–front and rear–front can be seen in figures 3(*a–c*) and 3(*d–f*), respectively, when the mixing length departs from the respective pure diffusive mixing lengths (stable case). As seen from figure 3(*a*), for $R_C = 2$, and for increasing of R_B from -1 until $R_B = 0.7$ onset of instability at the AB front delayed and after a critical $R_B \gtrsim 0.8$ (star-marked curve in figure 3*a*), the onset of instability reversed and became early. A similar trend occurs at the BC front as depicted in figure 3(*d*), i.e. the reversal of delayed onset to early onset occurs when $R_B \gtrsim 1.4$ (star-marked curve in figure 3*d*). However, for

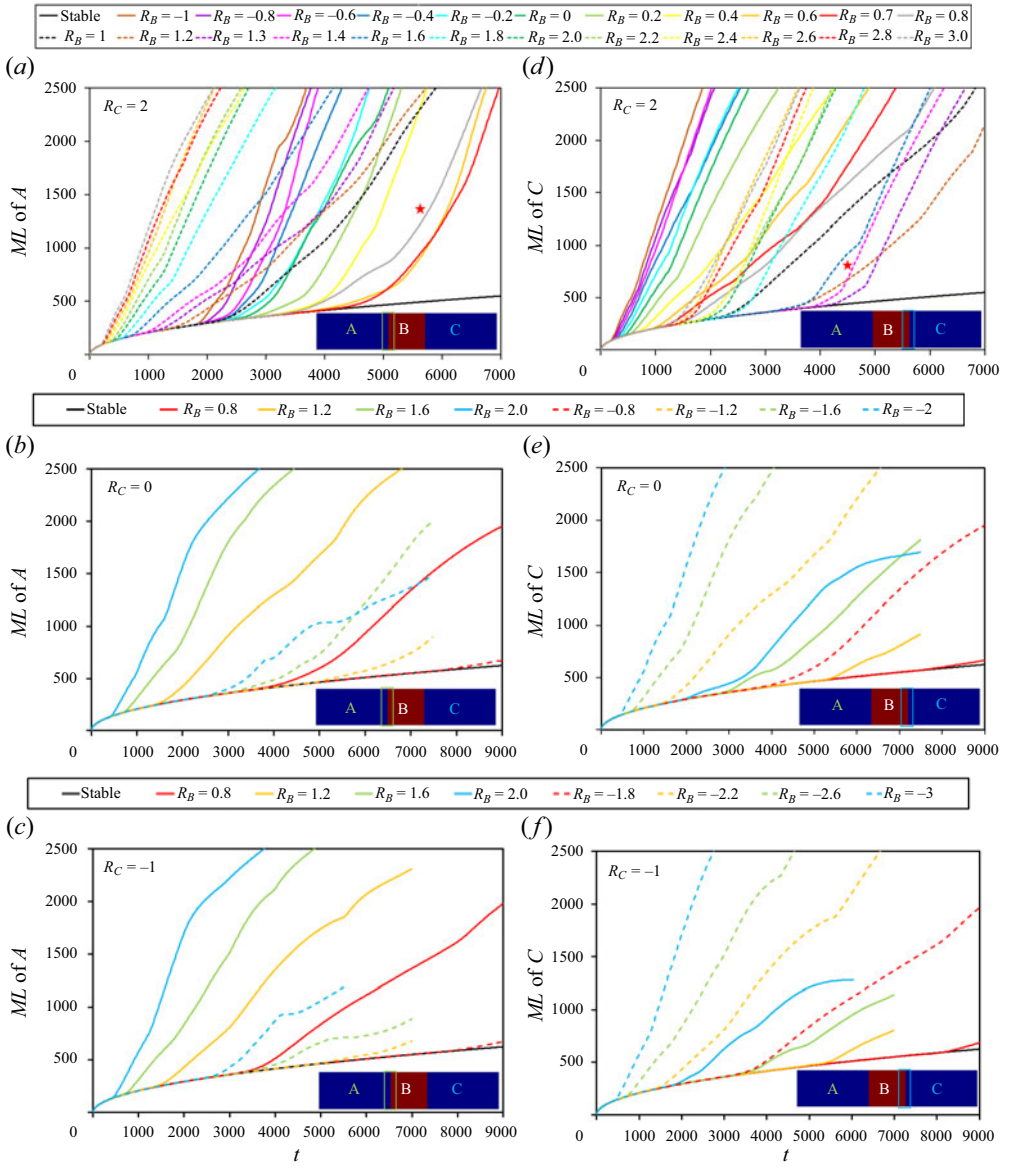

Figure 3. Mixing length of fluid (*a–c*) *A* and (*d–f*) *C* at R_C of 2, 0 and −1 for various values of R_B from one of the randomness case. The bottom black dashed line shows the pure diffusive mixing length of stable interfaces.

$R_C = 0$ and -1 when log mobility ratios $|R_B|$ increase and get farther away from R_A and R_C, the early onset is observed, and no reversal behaviour is seen on the onset of instability.

Further, the numerical simulation results for $R_C = 2$ with R_B of -0.4, 0.4, 1.0, 1.6 and 2.4 are depicted in figure 4 through the density plot of concentrations of species B. Initially, the frontal interface was unstable (e.g. see Supplementary movie 1 available at https://doi.org/10.1017/jfm.2024.670, with $R_B = 0.4$, $R_C = 2.0$), followed by the dual front (e.g. Supplementary movie 2, with $R_B = 1.0$, $R_C = 2.0$) and then the rear interface became unstable (e.g. Supplementary movie 3, with $R_B = 1.6$, $R_C = 2.0$). At a specific

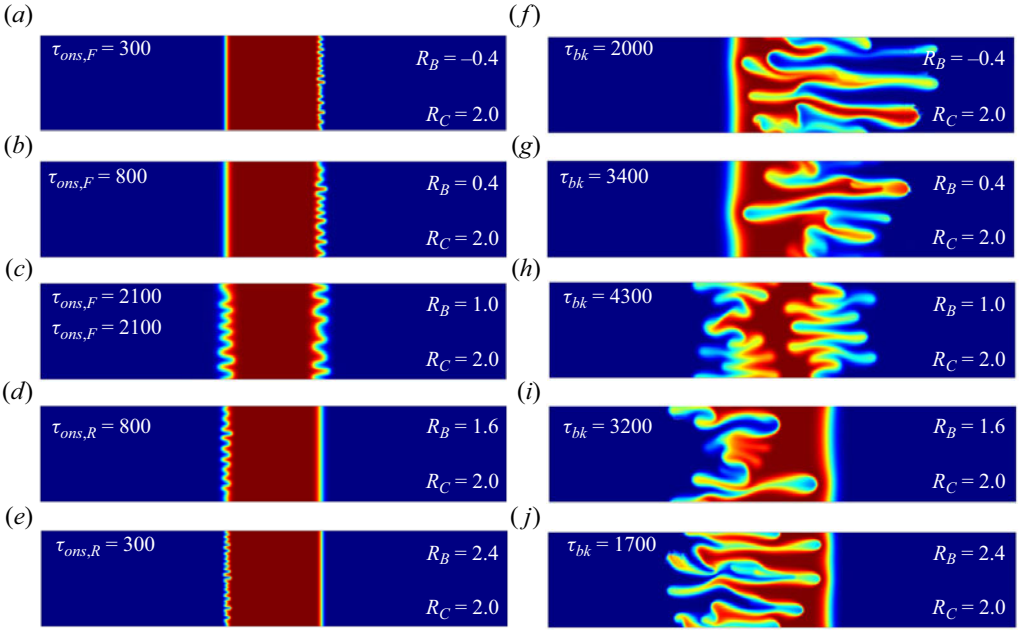

Figure 4. Numerical simulation results of $R_C = 2$ with various value R_B corresponding to the (*a–e*) $\tau_{on,R}$ or $\tau_{on,F}$ and τ_{bk} (*f–j*). Here R_B of −0.4 and 0.4 demonstrated a front-dominated fingering, whereas R_B of 1.6 and 2.4 demonstrated a rear-dominated fingering. Here R_B of 1.0, on the other hand, demonstrated a dual fingering.

time, the plots are shown representing the onset of VF front $\tau_{ons,R}$, $\tau_{ons,F}$ and breakthrough time τ_{bk}, which were chosen from the mixing length shown in figure 3.

With R_B of −0.4 (figure 4*a*,*f*), the rear interface is stable, whereas the front interface is unstable. As a result, the VF developed at the front interface and then disturbed the stable rear interface. For the R_B of 0.4 (figure 4*b*,*g*), similar phenomena with R_B of −0.4 also occur, but later. Even though both interfaces are unstable, the rear interface is more stable than the front interface due to the higher viscosity contrast between fluids *B* and *C* than fluids *A* and *B*. As a result, VF at the front interface occurred earlier and disturbed the rear interface before the instability grew. Similar but opposite phenomena also occur with R_B of 1.6 and 2.4 (figure 4*d*,*e*,*i*,*j*), in which the VF at the rear interface grew earlier and disturbed the front interface. These four cases demonstrate a single instability case with the R_B of −0.4 and 0.4 exhibiting front-dominated fingering and R_B of 1.6 and 2.4 exhibiting rear-dominated fingering, respectively. Although in R_B of 0.4 and 1.6, both interfaces are unstable, the more unstable interface disturbs the less stable interface before the instability at the less stable interface is developed. On the other hand, in the case R_B of 1.0 (figure 4*c*,*h*), both interfaces are equally unstable from the double instability. As a result, the VF started growing at the same time and finally collided, resulting in dual fingering. These instability dynamics can be divided into two types. The first type is the ordinary VF initiated by the interface viscosity contrast. The second type is not an instability (because the interface is stable) but rather a deformation initiated from VF of the other interface. Therefore, for this type, the onset time and the finger velocity of the other interface govern the onset of this instability mechanism.

Plotting $\tau_{ons,R}$, $\tau_{ons,F}$ and τ_{bk} with R_B in figure 5 provides a comprehensive point of view on the instability dynamics. By gradually increasing R_B from −1.0, $\tau_{ons,F}$ increases because the front interface is becoming more stable. Because this condition demonstrates

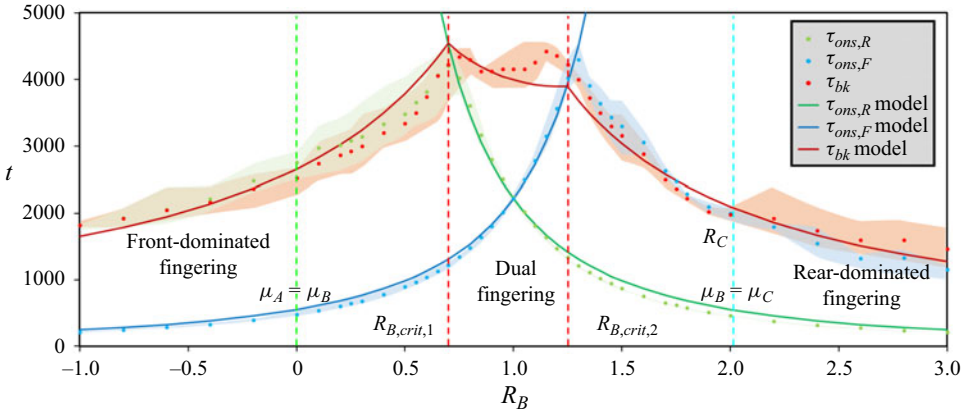

Figure 5. The $\tau_{ons,R}$, $\tau_{ons,F}$ and τ_{bk} of $R_C = 2$ at various R_B. Data points correspond to the averaged value from five simulations, and the colour-shaded area represents the data scattering of the five simulations. The solid lines represent the model from (3.1), (3.2) and (3.6). The green and the cyan dashed lines correspond to $\mu_A = \mu_B$ and $\mu_B = \mu_C$, respectively, whereas the red dashed lines correspond to both $R_{B,crit,1}$ and $R_{B,crit,2}$.

front-dominated fingering, $\tau_{ons,R}$ and τ_{bk} coincide, in which they also increase with R_B due to the delay in $\tau_{ons,F}$. When R_B is higher than 0.7, the delay on $\tau_{ons,F}$ provides sufficient time for the rear interface to develop instability. As a result, $\tau_{ons,R}$ becomes smaller than τ_{bk}, commencing the dual fingering regime. As $\tau_{ons,F}$ is getting delayed, when R_B is 1.0, $\tau_{ons,R}$ and $\tau_{ons,F}$ occur at relatively the same time. However, at R_B of 1.3, $\tau_{ons,F}$ and τ_{bk} start coinciding, marking the beginning of the rear-dominated fingering regime. Past this point, $\tau_{ons,R}$ keeps decreasing because the rear interface is getting less stable, and thus $\tau_{ons,F}$ and τ_{bk} also keep decreasing. Given these fingering dynamics, the τ_{bk} of 0.7 and 1.3 can be identified as the critical fluid B viscosity $R_{B,crit,1}$ and $R_{B,crit,2}$, in which the regime transition occurs.

These instability dynamics maps can be modelled by first generating the model for the onset time of both interface ($\tau_{ons,R}$ and $\tau_{ons,F}$), diffusion propagation (X_D) and both finger downstream and upstream velocities (V_+ and V_-). For the onset time, it decreases with the interface viscosity ratio by following the power function of minus two (Tan & Homsy 1988; De Wit *et al.* 2005) (figure 6*a*) as follows:

$$\tau_{ons,R} = 2215 R_B^{-2} \quad \text{for } R_B > 0, \tag{3.1}$$

$$\tau_{ons,F} = 2215 (R_C - R_B)^{-2} \quad \text{for } R_C - R_B > 0. \tag{3.2}$$

These models fit well with the data with a coefficient of determination (r^2) of 0.991 (see figure 6*a*). The green and blue solid lines in figure 5 clearly depict these models. The propagation of the diffusion fronts is modelled with a time square-root model by using the data of interface propagation at a stable state (figure 6*b*). The data fit well with a coefficient of determination (r^2) of 0.993. The corresponding model for the case of a pure diffusion front is given in (3.3) with the proportionality constant α as 3.29 when ϵ is chosen as 0.01. For the finger velocity, the upstream and downstream directions need to be modelled separately because the upstream finger velocity tends to be slower than the downstream finger velocity (Mishra *et al.* 2010; Nijjer, Hewitt & Neufeld 2018) (figure 6*c*). The finger velocity was calculated by measuring the required time for the finger to reach the other interface from its onset to its breakthrough, which can be obtained in the regimes of the front-dominated fingering and rear-dominated fingering by taking into account

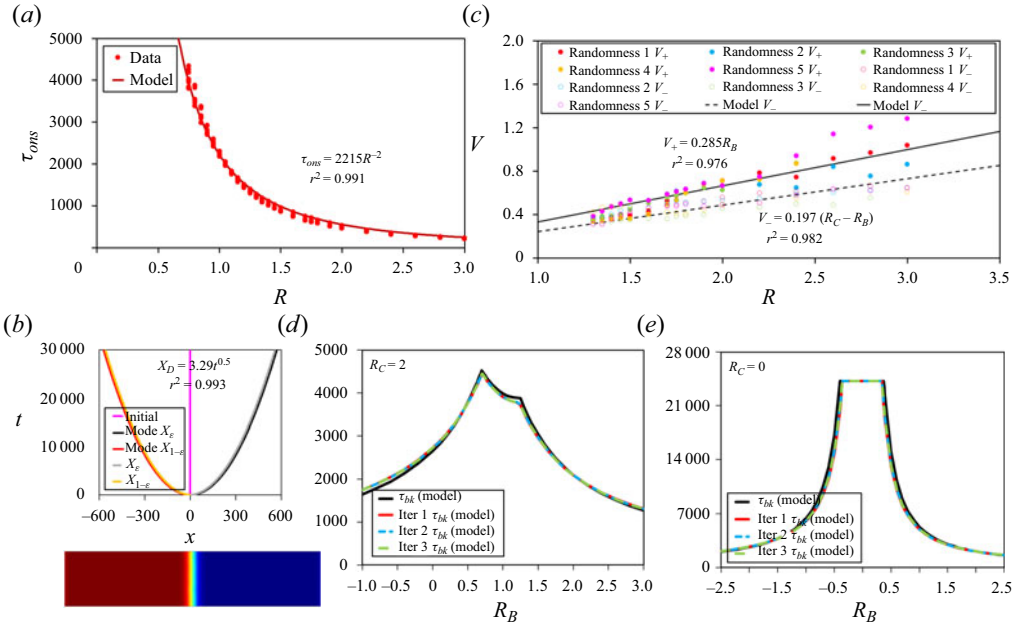

Figure 6. (*a*) The model formulation for $\tau_{ons,R}$ and $\tau_{ons,F}$ as shown in (3.1) and (3.2). (*b*) The model formulation for X_D as in (3.3). (*c*) The model formulation for (V_+) and (V_-) as shown in (3.4) and (3.5) and (*d*,*e*) the iteration process for τ_{bk} at (3.6)–(3.9) for R_C of 2 and 0.

the diffusion propagation as well. Because the diffusion propagation is independent of viscosity ratio but the finger velocity is a function of viscosity ratio (Nijjer *et al.* 2018), the following models were generated:

$$X_D(t) = X_\epsilon = X_{1-\epsilon} = \alpha t^{0.5} \quad \text{with } \alpha = f(\epsilon) = 3.29, \tag{3.3}$$

$$V_+ = 0.285R_B \quad \text{for } R_B > 0, \tag{3.4}$$

$$V_- = 0.197(R_C - R_B) \quad \text{for } R_B > 0, \tag{3.5}$$

where X_ϵ and $X_{1-\epsilon}$ are the locations of the maximum and minimum threshold concentration for mixing length, which is at $\epsilon = 0.01$. From these model equations ((3.3)–(3.5)), the breakthrough time τ_{bk}, as depicted by the solid red line in figure 5 on the three regimes of fingering dynamics, can be modelled with an equation as follows:

$$\tau_{bk} = \frac{W - X_D(t) + \tau_{ons,R}V_+ + \tau_{ons,F}V_-}{V_+ + V_-} \tag{3.6}$$

with

$$V_+ = 0 \quad \text{if } \tau_{ons,R} \geqslant \frac{W - X_D}{V_-} + \tau_{ons,F} \quad \text{at } R_{B,crit,1}, \tag{3.7}$$

$$V_- = 0 \quad \text{if } \tau_{ons,F} \geqslant \frac{W - X_D}{V_+} + \tau_{ons,R} \quad \text{at } R_{B,crit,2}, \tag{3.8}$$

$$\tau_{bk} = \left(\frac{W}{2\alpha}\right)^2 \quad \text{if } W \leqslant 2X_D. \tag{3.9}$$

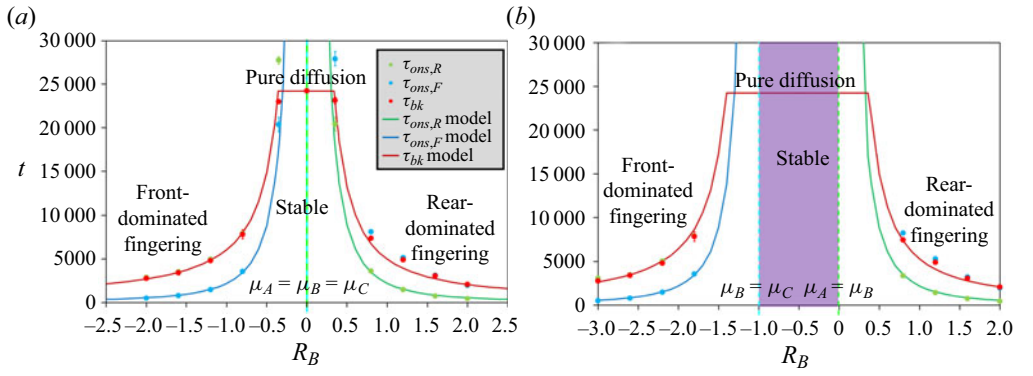

Figure 7. Onset and breakthrough time, $\tau_{ons,R}$, $\tau_{ons,F}$ and τ_{bk} of (*a*) $R_C = 0$ and (*b*) $R_C = -1$ at various R_B. Data points correspond to the average value of five simulations with the standard deviation. The solid lines represent the generated model from (3.1), (3.2) and (3.6). The green and the cyan dashed line correspond to $\mu_A = \mu_B$ and $\mu_B = \mu_C$, respectively, whereas the purple area corresponds to the stable regime.

Given the time variable presented in X_D at (3.3), which also contributes to breakthrough time τ_{bk}, hence, we calculate the breakthrough time τ_{bk} given in (3.6) using an iterative process with $X_D(t)$ given in (3.3) and defined as

$$\tau_{bk}^{j} = \frac{W - \alpha(t^j)^{0.5} + \tau_{ons,R}V_+ + \tau_{ons,F}V_-}{V_+ + V_-}, \tag{3.10}$$

$$\tau_{bk}^{j+1} = \frac{W - \alpha(\tau_{bk}^{j})^{0.5} + \tau_{ons,R}V_+ + \tau_{ons,F}V_-}{V_+ + V_-}. \tag{3.11}$$

We performed iterations considering the initial time as $t = 0$, and with three iterations, we achieved the convergence with a relative error of $O(10^{-4})$. The result of the breakthrough time obtained from the iteration process is shown in figures 6(*d*) and 6(*e*) for R_C of 2 and 0. We found that the value of τ_{bk} only changes slightly during each iteration. As for the pure diffusion condition given in (3.9), since it is only a function of the diffusion coefficient with a constant slice width of 1024, the τ_{bk} value is always fixed at 24 219 as also shown in figure 6(*e*).

As shown in figure 5, these models can predict the dynamics accurately. The $\tau_{ons,R}$ follows the model for $R_B \geqslant R_{B,crit,1}$, and the $\tau_{ons,F}$ follows the model for $R_B \leqslant R_{B,crit,2}$. The onset time beyond this condition no longer follows the model because the instability is not governed by viscosity contrast but by the disturbance from the other unstable interface. These models can also predict both $R_{B,crit,1}$ and $R_{B,crit,2}$ as the boundary between the three fingering regimes. The higher peak of τ_{bk} located at $R_{B,crit,1}$ corresponds to the slower V_- than the V_+, leading to later disturbance to the rear interface. The least accurate prediction is in the dual-fingering regime. Because the finger velocity models are based on the fully developed finger, these models cannot catch the early nonlinear finger dynamics near the onset. Given that two fingers were developing, this effect becomes more significant.

Now, for $R_C = 0$, the stability can also be divided into three regimes (figure 7*a*), but instead of dual fingering regime, a stable regime was found. Supplementary material (movie 4) provides the animations of stable flow dynamics with the condition of $R_B = -0.5$ and $R_C = -1.0$, which also helps to compare the different unstable regimes. At $R_B < 0$, the rear interface is stable, but the front interface is unstable, resulting in front-dominated fingering, whereas $R_B > 0$ shows the opposite, in which the rear interface

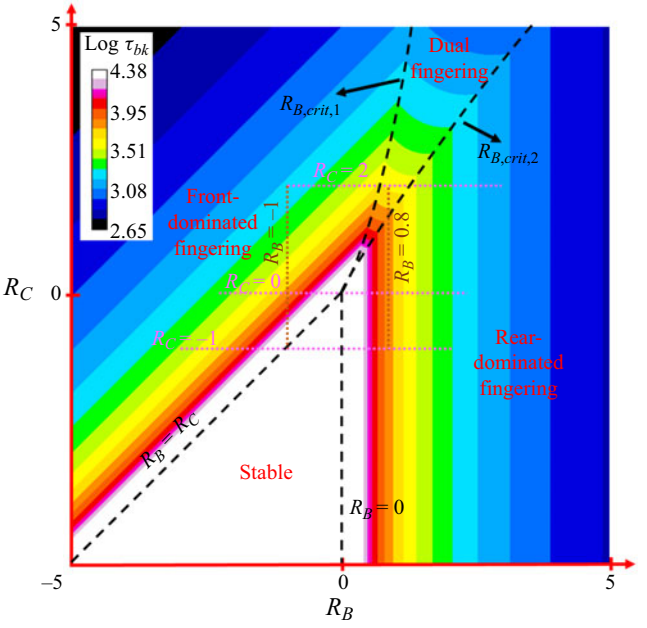

Figure 8. The regime map complemented with the τ_{bk} prediction for R_B of -5 to 5 and R_C between -5 and 5. The black dashed lines correspond to the regime boundary. The pink dotted lines correspond to the $R_C = 2$, $R_C = 0$ and $R_C = -1$, whereas the brown dotted lines correspond to $R_B = -1$ and $R_B = 0.8$.

is unstable, but the front interface is stable, corresponding to the rear dominated fingering. At $R_B = 0$, on the other hand, both interfaces are stable, resulting in a stable regime without $\tau_{ons,R}$ and $\tau_{ons,F}$. However, τ_{bk} can still occur due to the diffusion propagation, although at a much slower rate. Therefore, with R_B closing to 0, τ_{bk} increase sharply until it reaches a plateau of pure diffusion, spanning beyond the stable regime because breakthrough by diffusion propagation is still possible when the $\tau_{ons,R}$ and $\tau_{ons,F}$ occur late. This also serves as the τ_{bk} limit of the dual displacement system when τ_{bk} occurs due to diffusion propagation instead of VF interaction, as also given in (3.6). For $R_C = -1$, instability dynamics similar to those of $R_C = 0$ were also observed (figure 7*b*). The generated models of $\tau_{ons,R}$, $\tau_{ons,F}$ and τ_{bk} also demonstrate satisfying agreement with the data. The only difference is that the stable regime expands to R_B between 0 and -1.

Based on the developed models, the regime map complemented with the prediction of τ_{bk} can be created by extending the calculation for various R_B and R_C as shown in figure 8. Four regimes of rear-dominated fingering, dual fingering, front dominated fingering and stable are given. A stable regime is bound by the lines of $R_B = R_C$ and $R_B = 0$ and surrounded by the region of pure diffusion, as shown by the white-coloured area. The dual fingering regime is bound by the lines of $R_{B,crit,1}$ and $R_{B,crit,2}$ as given in (3.7) and (3.8). The remaining area corresponds to the front-dominated fingering at the left and rear-dominated fingering at the right.

In addition, further classification can be performed by fixing either R_B or R_C. The system with $R_C < 0$ is inherently stable because the system can become stable by changing R_B in between R_C and 0. In contrast, for $R_C > 0$, the configuration is inherently unstable because the system can never be stable unless the viscosity differences are very small, resulting in more dominant diffusion propagation than fingering. Similarly, by changing R_C, $R_B < 0$ is also inherently stable because it can be stable when R_C is lower than R_B, whereas $R_B > 0$ is

inherently unstable because there is no possibility of stable condition unless the viscosity differences are also very small. These conditions are also shown as pink and brown dotted lines in figure 8.

4. Conclusion

We modelled and mapped the stability dynamics of the VF interaction in dual displacement fronts. Four regimes were identified, and the τ_{bk} can be predicted in each regime. The models and map serve as design tools for harnessing the dual displacement fronts effectively, either for fluid displacement or fluid mixing, depending on its broad applications. We also believe that the models and map can be further developed in the future to explore the instability dynamics of the dual displacement fronts with other configurations. For example, with the different widths of the middle slice, the breakthrough time will be affected due to longer or shorter distances for finger movement and diffusion propagation. Although similar behaviour will still be observed, the regime map will change based on the width slice. Another example is chemical reactions at the interface since they can destabilize the interface or suppress finger development at one of the interfaces. Therefore, this work serves as the first exploration and findings on such an instability dynamics model and map from VF interaction.

Supplementary movies. Supplementary movies are available at https://doi.org/10.1017/jfm.2024.670.

Funding. We acknowledge Japan Society for the Promotion of Science for the funding support with the grant number of 22F22064 and fellowship opportunity for A.P.

Declaration of interests. The authors report no conflict of interest.

Author ORCIDs.
Aninditya Patmonoaji https://orcid.org/0000-0002-7031-9936;
Yuichiro Nagatsu https://orcid.org/0000-0003-2203-9830;
Manoranjan Mishra https://orcid.org/0000-0001-9933-5828.

References

Afzali, S., Rezaei, N. & Zendehboudi, S. 2018 A comprehensive review on enhanced oil recovery by water alternating gas (wag) injection. *Fuel* **227**, 218–246.

Bakharev, F., Enin, A., Groman, A., Kalyuzhnyuk, A., Matveenko, S., Petrova, Y., Starkov, I. & Tikhomirov, S. 2022 Velocity of viscous fingers in miscible displacement: comparison with analytical models. *J. Comput. Appl. Maths* **402**, 113808.

Cardoso, S.S.S. & Woods, A.W. 1995 The formation of drops through viscous instability. *J. Fluid Mech.* **289**, 351–378.

Chaudhuri, A. & Vishnudas, R. 2018 A systematic numerical modeling study of various polymer injection conditions on immiscible and miscible viscous fingering and oil recovery in a five-spot setup. *Fuel* **232**, 431–443.

Chen, C.Y., Huang, Y.C., Huang, Y.S. & Miranda, J.A. 2015 Enhanced mixing via alternating injection in radial Hele-Shaw flows. *Phys. Rev.* E **92**, 043008.

Coleman, J.T. & Sinton, D. 2005 A sequential injection microfluidic mixing strategy. *Microfluid Nanofluid* **1**, 319–327.

De Malsche, W., Op De Beeck, J., Gardeniers, H. & Desmet, G. 2009 Visualization and quantification of the onset and the extent of viscous fingering in sub- pillar columns. *J. Chromatogr. A* **1216**, 5511–5517.

De Wit, A. 2020 Chemo-hydrodynamic patterns and instabilities. *Annu. Rev. Fluid Mech.* **52**, 531–555.

De Wit, A., Bertho, Y. & Martin, M. 2005 Viscous fingering of miscible slices. *Phys. Fluids* **17**, 054114.

De Wit, A. & Homsy, G.M. 1999 Nonlinear interactions of chemical reactions and viscous fingering in porous media. *Phys. Fluids* **11**, 949–951.

GLASGOW, I. & AUBRY, N. 2003 Enhancement of microfluidic mixing using time pulsing. *Lab on a Chip* **3**, 114–120.

HASHIMOTO, M., GARSTECKI, P., STONE, H.A. & WHITESIDES, G.M. 2008 Interfacial instabilities in a microfluidic Hele-Shaw cell. *Soft. Matt.* **4**, 1403–1413.

HAUDIN, F., CALLEWAERT, M., DE MALSCHE, W. & DE WIT, A. 2016 Influence of nonideal mixing properties on viscous fingering in micropillar array column. *Phys. Rev. Fluids* **1**, 074001.

HEJAZI, S.H. & AZAIEZ, J. 2012 Stability of reactive interfaces in saturated porous media under gravity in the presence of transverse flows. *J. Fluid Mech.* **695**, 439–466.

HEJAZI, S.H., TREVELYAN, P.M.J., AZAIEZ, J. & DE WIT, A. 2010 Viscous fingering of a miscible reactive $A + B \rightarrow C$ interface: a linear stability analysis. *J. Fluid Mech.* **652**, 501–528.

HILL, S. 1952 Channelling in packed columns. *Chem. Engng Sci.* **1**, 247–253.

HOMSY, G.M. 1987 Viscous fingering in porous media. *Annu. Rev. Fluid Mech.* **19**, 271–311.

HOTA, T.K., PRAMANIK, S. & MISHRA, M. 2015 Stability of miscible displacements in porous media: rectilinear flow. *Phys. Rev.* E **92**, 2392–2398.

JHA, B., CUETO-FELGUEROSO, L. & JUANES, R. 2013 Synergetic fluid mixing from viscous fingering and alternating injection. *Phys. Rev. Lett.* **111**, 144501.

LE VAN, S. & CHON, B.H. 2017 Effects of salinity and slug size in miscible CO_2 water-alternating-gas core flooding experiments. *J. Ind. Engng Chem.* **52**, 99–107.

MACINNES, J.M., CHEN, Z. & ALLEN, R.W.K. 2005 Investigation of alternating-flow mixing in microchannels. *Chem. Engng Sci.* **60**, 3453–3467.

MAYFIELD, K.J., SHALLIKER, R.A., CATCHPOOLE, H.J., SWEENEY, A.P., WONG, V. & GUIOCHON, G. 2005 Viscous fingering induced flow instability in multidimensional liquid chromatography. *J. Chromatogr. A* **1080**, 124–131.

MISHRA, M., MARTIN, M. & DE WIT, A. 2008 Differences in miscible viscous fingering of finite width slices with positive or negative log-mobility ratio. *Phys. Rev.* E **78**, 066306.

MISHRA, M., MARTIN, M. & DE WIT, A. 2009 Influence of miscible viscous fingering of finite slices on an adsorbed solute dynamics. *Phys. Fluids* **21**, 083101.

MISHRA, M., MARTIN, M. & DE WIT, A. 2010 Influence of miscible viscous fingering with negative log-mobility ratio on spreading of adsorbed analytes. *Chem. Engng Sci.* **65**, 2392–2398.

NAGATSU, Y. & DE WIT, A. 2011 Viscous fingering of a miscible reactive $A + B \rightarrow C$ interface for an infinitely fast chemical reaction: nonlinear simulations. *Phys. Fluids* **23**, 043103.

NIJJER, J.S., HEWITT, D.R. & NEUFELD, J.A. 2018 The dynamics of miscible viscous fingering from onset to shutdown. *J. Fluid Mech.* **837**, 520–545.

PARASKEVA, C.A., CHARALAMBOUS, P.C., STOKKA, L., KLEPETSANIS, P.G., KOUTSOUKOS, P.G., READ, P., OSTVOLD, T. & PAYATAKES, A.C. 2000 Sandbed consolidation with mineral precipitation. *J. Colloid Interface Sci.* **232**, 326–339.

SAFFMAN, P.G. & TAYLOR, G.I. 1958 The penetration of a fluid into a porous medium or Hele-Shaw cell containing a more viscous liquid. *Proc. R. Soc. Lond.* A **245**, 73–94.

SHALLIKER, R.A., CATCHPOOLE, H.J., DENNIS, G.R. & GUIOCHON, G. 2007 Visualising viscous fingering in chromatography columns: high viscosity solute plug. *J. Chromatogr. A* **1142**, 48–55.

SHALLIKER, R.A. & GUIOCHON, G. 2010 Solvent viscosity mismatch between the solute plug and the mobile phase: considerations in the applications of two-dimensional HPLC. *Analyst* **135**, 222–229.

SHARMA, V., BIN OTHMAN, H., NAGATSU, Y. & MISHRA, M. 2021 Viscous fingering of miscible annular ring. *J. Fluid Mech.* **916**, A14.

TALAGHAT, M.R., ESMAEILZADEH, F. & MOWLA, D. 2009 Sand production control by chemical consolidation. *J. Petrol. Sci. Engng* **67**, 34–40.

TAN, C.T. & HOMSY, G.M. 1988 Simulation of nonlinear viscous fingering in miscible displacement. *Phys. Fluids* **31**, 1330–1338.

VISHNUDAS, R. & CHAUDHURI, A. 2017 A comprehensive numerical study of immiscible and miscible viscous fingers during chemical enhanced oil recovery. *Fuel* **194**, 480–490.

WOOD, M., SIMMONS, C.T. & HUTSON, J.L. 2004 A breakthrough curve analysis of unstable density-driven flow and transport in homogeneous porous media. *Water Resour. Res.* **40**, W03505.

YUAN, Q. & AZAIEZ, J. 2014 Cyclic time-dependent reactive flow displacements in porous media. *Chem. Engng Sci.* **109**, 136–146.